SRTTU

Journal of Electrical and Computer Engineering Innovations
(JECEI)
Journal homepage: http://www.jecei.sru.ac.ir

JECEI

Research paper

Design and Optimization of a Counter-Rotating Double-Rotor Synchronous Motor with a Permanent Magnet External Rotor and a Reluctance Internal Rotor

Pouria Nadri [1], ***Behrooz Rezaeealam*** [1,*], ***Morteza Mikhak-Beyranvand*** [2]

[1] *Department of Electrical Engineering, Faculty of Engineering, Lorestan University, Khorramabad, Lorestan, Iran.*
[2] *Department of Electrical Engineering, Technical and Vocational University (TVU), Tehran, Iran.*

Article Info

Article History:
Received 12 January 2026
Reviewed 17 March 2026
Revised 19 May 2026
Accepted 26 May 2026

Keywords:
Counter-Rotating Dual-Rotor synchronous motor
Cogging torque
Taguchi method
Finite Element Analysis (FEA)
Torque ripple

*Corresponding Author's Email Address: *rezaee.bh@lu.ac.ir*

Abstract

Background and Objectives: Dual-rotor synchronous motors with counter-rotation are of significant interest for electric machine design due to their high performance and specific applications. In this study, a new Counter-Rotating Dual-Rotor Synchronous Motor (CRDRSM) is presented, with the permanent magnet (PM) rotor as the outer rotor and the reluctance rotor as the inner rotor.

Methods: To identify the optimal structure, the effects of distributed and fractional-pitch windings are first compared. Then, various PM and reluctance rotor topologies are examined in order to select the optimal combination. Despite high output torque, cogging torque significantly affects motor performance; therefore, reducing cogging torque is the main concern of this research. Dimensional optimization is conducted using the Taguchi method to minimize cogging torque in the PM rotor. Four key design parameters, including the PM arc, PM thickness, stator opening slot, and stator tooth width, are selected as optimization variables, while other parameters are kept constant. The minimum and maximum ranges of these variables are determined using parametric scanning and ANSYS Maxwell finite element software. Briefly, the optimization process proceeds in three stages: (1) winding configuration comparison, (2) selection of optimal inner and outer rotor structures, and (3) dimensional optimization using the Taguchi method.

Results: Analysis of the results demonstrates that the cogging torque of the proposed motor is reduced by up to 62.36%, the output power and efficiency are increased, and the voltage THD is also reduced. Other performance characteristics, including output torque and electromagnetic stability, are improved compared to the initial design or remain at a desirable level.

Conclusion: Finite Element Analysis (FEA) demonstrated that the distributed winding configuration delivers the best performance among all tested options. Model C, featuring a hyperbolic-line reluctance inner rotor combined with a surface-mounted PM outer rotor, was identified as the best configuration. This model offers an excellent balance of high torque, low torque ripple, minimized back-EMF harmonics, and satisfactory efficiency, making it highly suitable for submarine propulsion systems. To further reduce cogging torque (one of the primary sources of torque ripple and acoustic noise), the motor geometry was optimized using the Taguchi method and FEA. Overall, the electromagnetic performance of the proposed CRDRSM was validated in terms of flux density distribution, output torque, and cogging torque.

How to cite this paper:
P. Nadri, B. Rezaeealam, M. Mikhak-Beyranvand, "Design and optimization of a counter-rotating double-rotor synchronous motor with a permanent magnet external rotor and a reluctance internal rotor," J. Electr. Comput. Eng. Innovations, 14(2): 449-464, 2026.

DOI: 10.22061/jecei.2026.12667.901

URL: https://jecei.sru.ac.ir/article_12562.html

Introduction

CRDRSMs have emerged in recent years as an attractive option for applications with space constraints, high torque density requirements, dynamic performance, and optimal efficiency [1], [2]. They have garnered attention in applications such as the marine industries, aviation, hybrid electric vehicles, and underwater vehicle propulsion systems [1]-[4]. Compared to dual-rotor motors, single-rotor motors increase the mechanical stresses on the rotor surface due to their integrated structure and larger rotor diameter. However, in dual-rotor motors, by utilizing an inner rotor with a smaller diameter and an outer rotor, mechanical stresses, acoustic noise, and torque ripple are reduced. In CRDRSMs, by using the technique of reverse rotation of two rotors, the problems caused by unidirectional rotation and enable the movement of reverse rotation propellers [5]. Dual-rotor counter-rotating machines are divided into two main types: dual-rotor electric machines with a common stator and dual-rotor electric machines without a stator. The main difference between these two types is in mechanical power [6]. A dual-rotor motor with a shared stator can provide different speeds and torques for each rotor, whereas in a stator-less motor, the torques of the two rotors must be equal, although the speeds can differ [5]-[7]. In underwater vehicles, electric propulsion systems offer superior performance due to their higher efficiency, better controllability, simpler maintenance, and lower acoustic noise compared to thermal propulsion systems. In the military industries, special attention has also been given to electric propulsion in modern vessels and ships, as this architecture offers greater flexibility, efficiency, and fault tolerance compared to mechanical propulsion systems [8].

In the fast-paced world of technology and industry, the need for high-performance and energy-efficient electric motors is increasingly felt. In this context, Permanent Magnet Synchronous Motors (PMSM) and Switched Reluctance Motors (SRM) have found a special place as two modern and innovative options in the design and development of electric motors [9], [10]. PMSMs provide high performance without the need for a mechanical commutator and have advantages such as small size, low weight, low losses, high efficiency, and high torque density, making them very suitable for space-constrained applications, such as submarine propulsion [11], [12]. Additionally, SRMs have been proposed as an alternative to reduce the use of PMs due to their simple mechanical design, low cost, and high reliability, while providing acceptable output torque [12]-[14].

The design and optimization of a dual-rotor hybrid motor (reluctance-PM) using the reverse rotation technique can be an attractive and unique idea in the development of electric motors. In [12], a synchronous dual-rotor motor with a PM outer rotor and a reluctance inner rotor has been introduced that includes a magnetic insulation ring in the middle of the stator yoke, aiming to reduce the cogging torque.

In order to increase the torque density and to reduce torque ripple, this paper proposes a CRDRSM, which utilizes a radial flux configuration and includes an outer rotor with surface PMs, an inner rotor of the reluctance type, and a common stator located between them. Then, an attempt is made to minimize the torque ripple of the proposed CRDRSM for applications that require low noise levels [5], [15]. Moreover, it seems that the thermal behavior of the proposed CRDRSM will improve, as the inner rotor does not include PMs.

Cogging torque in PM motors is caused by the interaction between the magnets and the stator slots, leading to torque ripple and acoustic noise [16]. Various methods have been proposed to reduce cogging torque, including stator slotting [17] and rotor structure optimization [18]. There are well-established design optimization techniques for electrical machines, including deterministic methods [19], stochastic methods (such as genetic algorithms) [20], and intelligent methods [21].

Besides, many papers have employed the Taguchi method for design optimization of PM motors in order to reduce cogging torque [22]-[24]. In [23] and [24], the Taguchi method has been used with the FEA to evaluate the cogging torque due to PM tolerances, by which the sampling number has been reduced significantly. The Taguchi optimization method, by defining a loss function and analyzing the impact of various factors on the output, makes it possible to determine optimal parameters under conditions with the least sensitivity to environmental noise and unwanted variations [25]-[27]. Considering the complex nature of modeling in dual-rotor synchronous motors, the use of the Taguchi analysis method combined with parameter displacement analysis leads to the rapid and precise identification of key parameters affecting motor performance [28]. In addition to significantly reducing optimization time and costs, it also enhances key parameters such as increased efficiency, reduced cogging torque, and improved output torque quality, ultimately improving electromagnetic performance [29]-[31].

In this study, the Taguchi method was chosen due to its high efficiency in reducing computation time and requiring fewer samples compared to other methods, such as PSO [30]. This method is based on the design of orthogonal experiments and allows for finding the optimal combination of design variables with minimal calculations [28], [29], [31].

This research, using FEA in the commercial software ANSYS Maxwell, first compares two types of windings (distributed and fractional pitch) and selects the most suitable winding. Then, eight different configurations for combining reluctance rotors and PMs are examined, and the optimal model is selected. Since cogging torque significantly affects torque ripple and output torque quality, geometric optimization has been carried out with the aim of reducing the cogging torque of the external PM rotor. The optimization range of parameters has been determined considering the motor dimension constraints, and by combining the Taguchi analysis method and parameter displacement, the optimal parameters for reducing cogging torque have been extracted. Simulation analyses confirm the effectiveness of the optimization. Ultimately, the magnetic field analysis, stator yoke flux density, air gap flux density, inductance, electromotive force (EMF), output torques, power, and efficiency confirm the proper performance of the proposed motor.

Motor Preliminary Design

A. Motor Topology

In this research, a CRDRSM has been proposed and investigated, which includes an outer rotor with surface PMs and an inner rotor of the reluctance type. This motor has a common stator located between two concentric rotors. Both rotors rotate at the same speed but in opposite directions. Slots are embedded in the inner and outer surfaces of the stator, between which the stator windings are distributed. To create rotating magnetic fields with opposite directions in the inner and outer air gaps of the stator, a phase shift between the windings of the outer and inner layers of the stator has been applied. This phase displacement results in the generation of two opposing magnetic driving forces in the inner and outer air gaps. Fig. 1 shows a schematic view of the proposed motor.

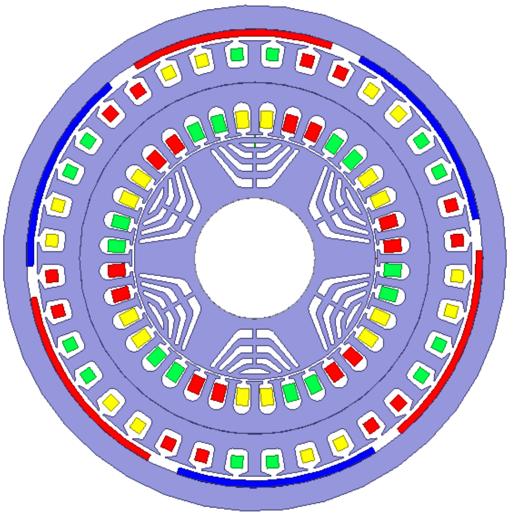

Fig. 1: Proposed structure of CRDRSM.

In fact, this motor can be described as a combination of a synchronous reluctance motor and a PM motor, benefiting from the advantages of both. The main geometric and electrical parameters considered for the initial model are summarized in Table 1.

Table 1: Design Dimensions and Main Parameters of CRDRSM

Parameter	Value
Number of phases	3
Number of poles	6
Number of slots	36
Rated frequency (Hz)	50
Stator winding connection	Y
Effective length (mm)	198
Inner radius of stator (mm)	61
Outer radius of stator (mm)	108
Radius of outer rotor (mm)	110
Radius of inner rotor (mm)	60
Inner air-gap length (mm)	1
Outer air-gap length (mm)	2
Speed (rpm)	1000
PM type	NdFeB-N35

The proposed motor has 36 slots and 6 poles, which provides a balanced three-phase winding layout and ensures both rotors perform properly. This selection results in an integer slots-per-pole-per-phase value of $q = \frac{Q}{mP} = \frac{36}{6\times3} = 2$, which is a common choice for distributed windings and contributes to stable electromagnetic performance. In the CRDRSM motor, the number of poles in the inner rotor (reluctance) and the number of poles in the outer rotor (PM) must be equal to achieve balance. The initial parameter set in Table 1 was selected to satisfy the required operating conditions and dimensional constraints.

In the CRDRSM motor, the number of poles in the inner rotor (reluctance) and the number of poles in the outer rotor (PM) must be equal to achieve balance.

B. Motor Power Equation

I. External PM Motor

The rated output power of a PM motor depends on voltage, current, and the number of phases. Considering that the waveforms of stator current and voltage are usually non-sinusoidal, a shape coefficient ($\mathrm{k_p}$) is taken into account for the precise calculation of output power. Assuming the neglect of losses due to winding impedance and leakage inductance, the output power of the external PM motor ($\mathrm{P_{spm}}$) is expressed as:

$$P_{spm} = \eta m k_p E_{pk} I_{pk} \tag{1}$$

where η is the motor efficiency, m is the number of phases, $\mathrm{k_p}$ is the shape coefficient, $\mathrm{E_{pk}}$ is the peak value of the single-phase back electromotive force (EMF), and I_{pk} is the peak value of the stator phase current. Assuming the stator current vector is aligned with the back EMF vector, the d-axis current would be zero, and the shape coefficient (k_p) is considered to be 0.5. The peak value of the back EMF of the outer PM motor is obtained from the induced electromotive force (E = BLV), where B is the magnetic flux density, L is the effective length of the winding, and V is the linear speed of the winding in the magnetic field. The linear speed in the outer air gap is calculated using the relation $V = 2\pi\frac{D_{os}}{2}\left(\frac{f_e}{p}\right)$, where D_{os} is the outer diameter of the stator, f_e is the supply frequency, and p is the number of pole pairs. Therefore, the peak back EMF value is expressed as:

$$E_{pk} = \pi K_w N_t B_{gl.p}\left(\frac{f_e}{p}\right) D_{os} L_e \tag{2}$$

where K_w is the winding factor, N_t is the number of turns of the winding in each phase, $B_{gl.p}$ is the peak value of the air gap flux density of the surface-mounted PM rotor, L_e is the axial length of the motor core, and f_e/p is the angular speed of the magnetic field. The peak phase current (I_{pk}) is also calculated from [32]:

$$I_{pk} = \frac{\sqrt{2}D_{os}\pi}{mN_t} A_{sp.rms} \tag{3}$$

where $A_{sp.rms}$ is the electrical load value on the PM rotor side, m is the number of phases, D_{os} is the outer diameter of the stator, and N_t is the number of turns of the winding in each phase. By substituting (2) and (3) into (1), the output power of the external PM motor is obtained as:

$$P_{spm} = \frac{\sqrt{2}\pi^2}{2} K_w \eta \left(\frac{f_e}{p}\right) B_{gl.p} A_{sp.rms} D_{os}^2 L_e \tag{4}$$

II. Internal Reluctance Motor

For the synchronous reluctance motor (SynRM), the output torque is provided by the components of the d-axis and q-axis currents, and the output power is affected by the power factor ($\cos(\gamma)$). Unlike a PM motor, the reluctance rotor lacks a PM and therefore does not generate direct back EMF. As a result, the output power P_{syr} of the synchronous reluctance motor can be expressed as:

$$P_{syr} = \frac{\sqrt{2}\pi^2}{2} K_w \eta \left(\frac{f_e}{p}\right) \cos(\gamma)\, B_{g1.R} A_{sR.rms} D_{is}^2 L_e \tag{5}$$

that $\cos(\gamma)$ is the power factor of the internal reluctance motor, γ is the angle between the stator current and the q-axis component, $B_{gl.R}$ is the peak value of the air gap magnetic flux density, $A_{sR.rms}$ is the electrical load value on the reluctance rotor side, and D_{is} is the inner diameter of the stator. (5) is derived from the classical electromagnetic power formulation of synchronous machines based on shear stress theory, in which the output power is expressed as a function of the air-gap magnetic loading, stator electrical loading, and active machine volume, while standard coefficients account for sinusoidal field distributions and peak-to-RMS conversions.

III. Double Rotor Motor

By combining the equations of the external PM motor and the internal reluctance motor, the total power of the CRDRSM is obtained as:

$$\begin{aligned} P_{total} &= \frac{\sqrt{2}\pi^2}{2} K_w \eta \left(\frac{f_e}{p}\right) L_e \big[B_{g1.R} A_{sR.rms} D_{is}^2 \cos\gamma \\ &\qquad + B_{g1.p} A_{sp.rms} D_{os}^2\big] \end{aligned} \tag{6}$$

Considering the series connection of the internal and external stator windings, the winding currents are equal, and therefore:

$$\frac{A_{sp.rms} D_{os}\pi}{mN_t} = \frac{A_{sR.rms} D_{is}\pi}{mN_t} \tag{7}$$

By simplifying (7), the relationship between the effective electrical loads of the inner and outer rotors with the diameter ratio is obtained as:

$$A_{sp.rms} = \frac{D_{is}}{D_{os}} A_{sR.rms} \tag{8}$$

By substituting (8) into (6), and after simplification, the total motor power (P_{total}) can be expressed as:

$$\begin{aligned} P_{total} &= \frac{\sqrt{2}\pi^2}{2} K_w \eta \left(\frac{f_e}{p}\right) \Big[B_{g1.R} \cos\gamma \\ &\qquad + B_{g1.P} \frac{D_{os}}{D_{is}}\Big] A_{sR.rms} D_{is}^2 L_e \end{aligned} \tag{9}$$

The electromagnetic torque of the motor consists of a constant component (DC) and oscillating components (ripple) expressed as:

$$T_{(t)} = T_{DC} + \sum T_n \sin(n\omega t + \varphi n)\, T_{(t)} \tag{10}$$

that T_{DC} is the average torque, and T_n are the harmonic components that produce torque ripple. For the various topologies presented in this research, the ripple percentage of the torque is calculated as:

$$Ripple\ Torque\ (\%) = \frac{T_{rms\ AC}}{T_{DC}} \times 100 \tag{11}$$

where $T_{rms\ AC}$ is the effective value of the alternating torque.

According to the above equations, the extractable powers from the two rotors can be examined, based on which the overall geometric dimensions of the two rotors and the stator can be determined.

Comparison of Rotor Structures and Winding Types

A. Comparison of Winding Types for CRDRSM

In this section, two types of distributed and fractional-pitch windings for the CRDRSM with an outer PM rotor and an inner reluctance rotor have been designed and evaluated using FEA in ANSYS Maxwell software. The aim of this analysis is to select the most suitable winding type for the proposed CRDRSM based on key performance criteria such as output torque, torque ripple, Total Harmonic Distortion (THD) of no-load voltage, and efficiency, with an emphasis on submarine propulsion applications that require high torque and low noise [5], [15].

I. *Design and evaluation of winding types*

The two types of winding examined are:

- Distributed winding: The phases of a single-phase winding are distributed across several stator slots, resulting in a more uniform magnetic field and sinusoidal back EMF [33], [34].
- Fractional pitch winding: The number of slots per pole per phase is fractional, which creates a specific distribution of the magnetic field and reduces the cogging torque [33], [35].

The proposed CRDRSM has a 36-slot stator. In Fig. 2, the winding layout of slots 1 to 18 is illustrated for both distributed and fractional-pitch windings. Evidently, the winding pattern of slots 19 to 36 is a periodic repetition of the same arrangement shown in slots 1 to 18. The simulations were conducted using ANSYS Maxwell, and key parameters such as torque, torque ripple, THD, EMF, current, output power, losses, and efficiency were extracted.

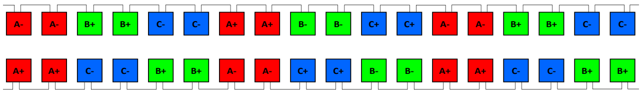

(a) Distributed winding

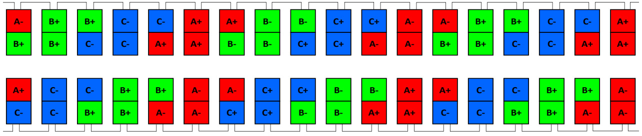

(b) Fractional-pitch winding

Fig. 2: Comparison of distributed and fractional-pitch winding types for CRDRSM.

Fig. 3 shows the proposed CRDRSM's distributed and fractional pitch winding patterns (for phase A).

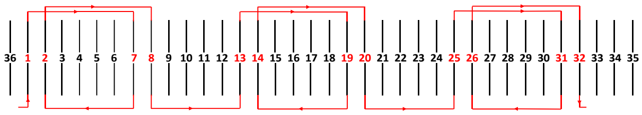

(a) Distributed winding

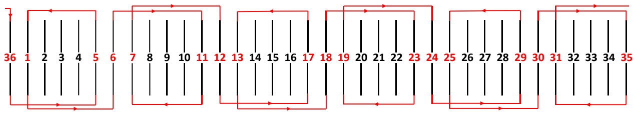

(b) Fractional-pitch winding

Fig. 3: Comparison of phase A winding pattern for distributed and fractional-pitch windings for CRDRSM.

For clarity, the specifications of the distributed and fractional-pitch windings are shown in Table 2.

Table 2: Detailed specifications of distributed and fractional-pitch windings for CRDRSM

Parameters	Distributed	Fractional-pitch
Winding type	Full-pitch	Short-pitch
Layer arrangement	Single-layer	Double-layer
Electrical angle of short pitch	0°	30°
Slots per pole per phase (q)	2	2
Coil pitch (in slots)	6	5
Distribution factor	0.9659	0.9659
Pitch factor	1	0.9659
Winding factor	0.9659	0.9330
Connection type	Y-connected	Y-connected

II. *Simulation Results and Optimal Selection*

Table 3 compares the simulation results of two types of windings for the proposed CRDRSM. Based on the data in Table 3, Fig. 4 depicts the values of the internal torque, external torque, external torque ripple, and internal torque for distributed winding and fractional-pitch winding.

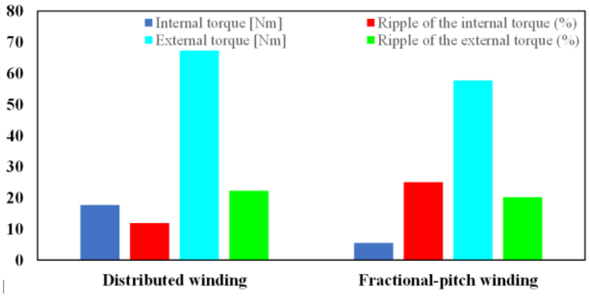

Fig. 4: Torque and torque ripple comparison for the suggested windings. (for internal and external rotors).

Table 3: Comparison of results for different types of winding

Parameters	Distributed	Fractional-pitch	Unit
Torque $_{\text{Internal}}$	17.7	5.54	Nm
Torque $_{\text{External}}$	-67.27	-57.7	Nm
Ripple T $_{\text{Internal}}$	11.88	25.06	%
Ripple T $_{\text{External}}$	22.24	20.19	%
THD V_{NL}	23.29	19.38	%
Harmonic V_{NL}	116.8	112.86	V
EMF_{rms}	193.04	192.37	V
I_{rms}	18.97	17.49	A
$P_{\text{out-put}}$	8.9	6.62	KW
η	87.36	85.55	%

Accordingly, the distributed winding was chosen as the most suitable option for CRDRSM. This selection has been made based on the following key criteria:

- High torque: The distributed winding with an internal torque of 17.7 Nm and the external torque of -67.27 Nm is significantly higher than a fractional pitch winding (internal torque of 5.54 Nm and the external torque of -57.7 Nm), making it suitable for submarine propulsion applications that require high torque [5], [15].
- Low torque ripple: The internal torque ripple (11.88%) in the distributed winding is significantly lower than the internal torque ripple (25.06%) in the fractional pitch winding. Also, the external torque ripple of both windings is close to each other. ensuring smoother operation and reduced acoustic noise, a critical feature for noise-sensitive applications [15].
- Acceptable THD: Although the THD of back EMF in the distributed winding (23.29%) is higher than that of the fractional pitch (19.38%), it improves the overall motor performance due to the production of sinusoidal back EMF [34].
- Balance of efficiency and power: An efficiency of 87.36% in the distributed winding is higher than the fractional pitch winding (85.55%), is justifiable for high-power applications due to the higher torque and lower ripple [34].

For better comparison of the results, the torque versus time curve under transient and steady-state conditions for distributed winding and fractional-pitch winding is shown in Fig. 5.

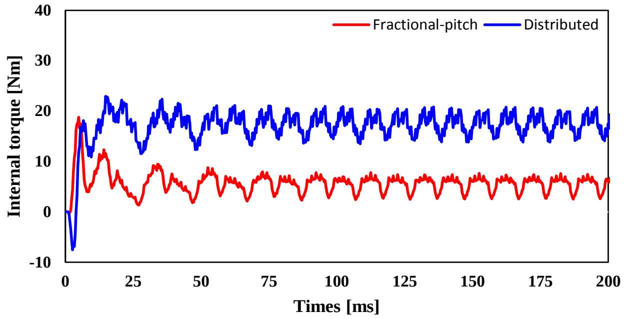

(a) Internal torque

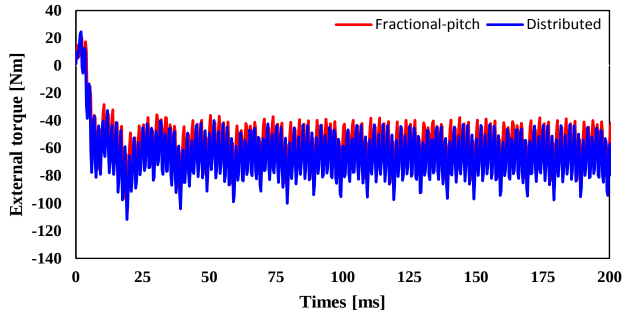

(b) External torque

Fig. 5: Curve of the torque versus time in transient and steady-state conditions for fractional-pitch and distributed windings.

Distributed winding, by creating a more uniform magnetic field and reducing torque ripple, helps optimize cogging torque in the later stages of CRDRSM design, especially for the outer PM rotor [34]. This feature, along with thermal stability and smooth operation, makes it ideal for underwater applications that require high torque and low noise [5], [15]. Therefore, considering the balance between torque, torque ripple, and stability, the distributed winding was chosen as the best option for the proposed CRDRSM.

B. Optimal Selection of Rotor Structures for CRDRSM

In this section, various combinations of internal rotor (reluctance) and external rotor (PM) for CRDRSM have been designed and evaluated using distributed winding. The goal is to select the optimal structure among the eight proposed combinations using FEA in ANSYS Maxwell software. These combinations include two types of external rotors (surface PM and internal PM or insert) and four types of reluctance internal rotors (ALA, hyperbolic, hyperbolic-line, and concentric-polyline). Fig. 6 shows these eight structures as follows:

- Model A: ALA Reluctance Rotor with Surface PM Rotor.
- Model B: Hyperbolic Reluctance Rotor with Surface PM Rotor.
- Model C: Hyperbolic-Line Reluctance Rotor with Surface PM Rotor.
- Model D: Concentric-Polyline Reluctance Rotor with Surface PM Rotor.
- Model E: ALA Reluctance Rotor with Internal PM Rotor.
- Model F: Hyperbolic Reluctance Rotor with Internal PM Rotor.
- Model G: Hyperbolic-Line Reluctance Rotor with Internal PM Rotor.
- Model H: Concentric-Polyline Reluctance Rotor with Internal PM Rotor.

The lengths of inner and outer air gaps are the same for all models in Fig. 6 (Models A to H), meaning the inner air gap length for all models is one millimeter, and the outer air gap length for all models is two millimeters.

The simulation results for key metrics such as torque, torque ripple, THD of no-load voltage, EMF, current, inductance, output power, losses, and efficiency are presented in Table 4.

This analysis has been conducted with a focus on submarine propulsion applications that require high torque and low noise [5], [15].

Compared to the surface-type PM, the insert-type PM generates a larger air gap for the internal stator winding to produce flux, and consequently, the surface-type PM is favored above the insert-type PM when choosing the optimal model. Because of this, models B and C outperform the other models, as shown in Table 4.

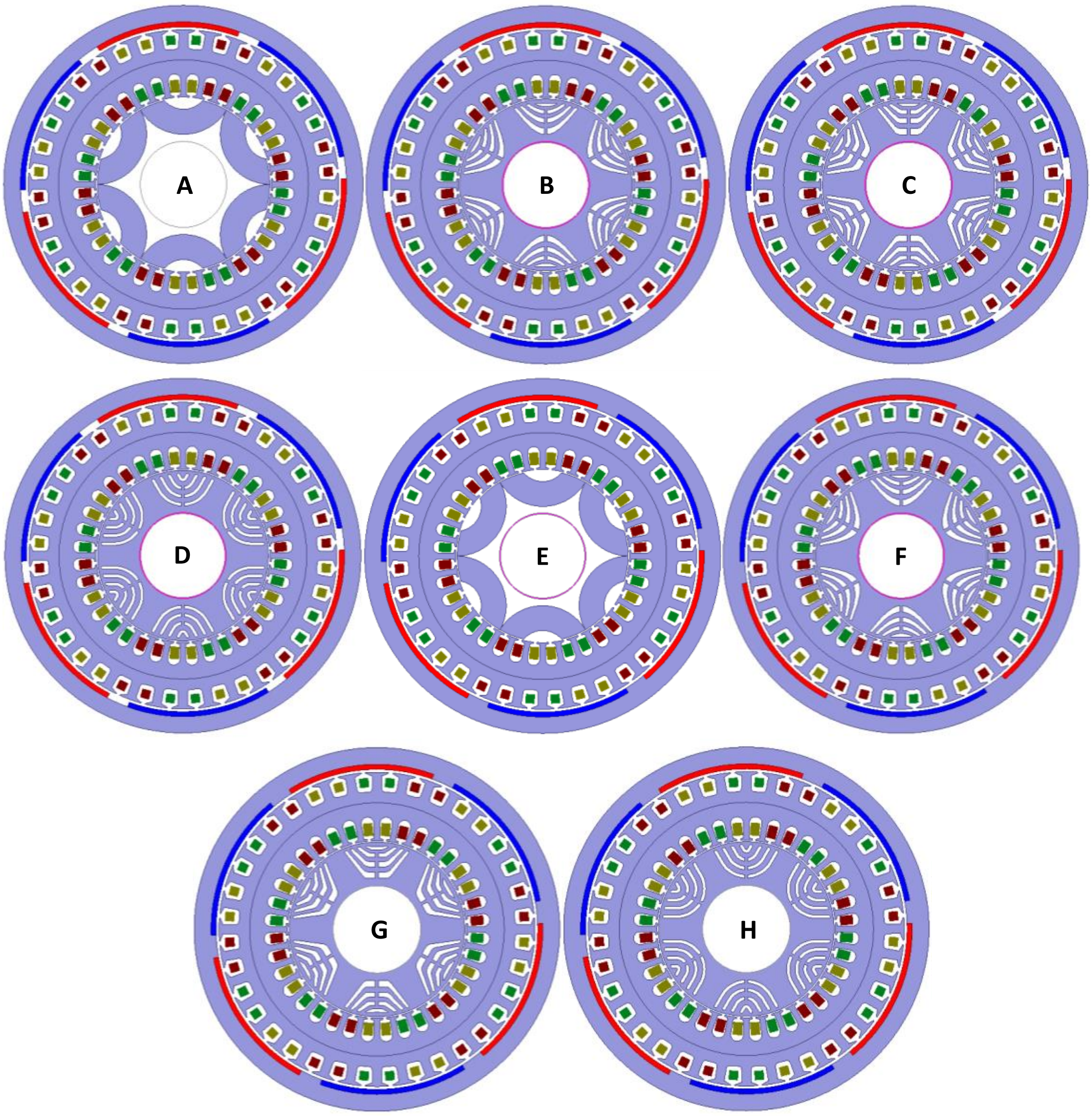

Fig. 6: Comparison of different topologies for a combined dual rotor (Reluctance-PM) counter-rotating motor.

Table 4: Comparison of results obtained from different proposed topologies

Parameters	Model A	Model B	Model C	Model D	Model E	Model F	Model G	Model H	Unit
Cogging $_{\text{Zero-Peak}}$	4.28	4.41	4.41	4.41	3.89	3.38	3.38	3.38	Nm
Torque $_{\text{Internal}}$	24.61	17.84	17.7	14.03	23.72	17.45	17.32	13.81	Nm
Torque $_{\text{External}}$	-73.92	-67.28	-67.27	-66.59	-74.20	-67.98	-67.97	-66.87	Nm
Ripple T $_{\text{Internal}}$	18.84	11.87	11.88	12.73	19.11	12.36	12.37	13.17	%
Ripple T $_{\text{External}}$	22.11	22.26	22.24	21.95	28.49	27.75	27.73	26.85	%
THD V_{NL}	19.32	20.2	23.29	20.2	19	18.89	23.83	32	%
Harmonic V_{NL}	114.3	115.8	116.8	116.5	108.4	114.5	95	84.77	V
EMF_{rms}	193.08	193.02	193.04	193.02	202.11	201.9	201.9	201.9	V
I_{rms}	21.88	19	18.97	18.17	21.51	18.84	18.82	18.03	A
$P_{out\text{-}put}$	10.31	8.91	8.9	8.44	10.25	8.94	8.93	8.49	KW
η	86.15	87.3	87.36	87.48	86.8	87.89	87.89	88.24	%

Thus, model C is chosen as the best motor even though the results are close to one another. Based on the information in Table 4, Fig. 7 depicts the values of the internal torque, external torque, external torque ripple, and internal torque ripple of the topologies shown in Fig. 6 (Models A through H).

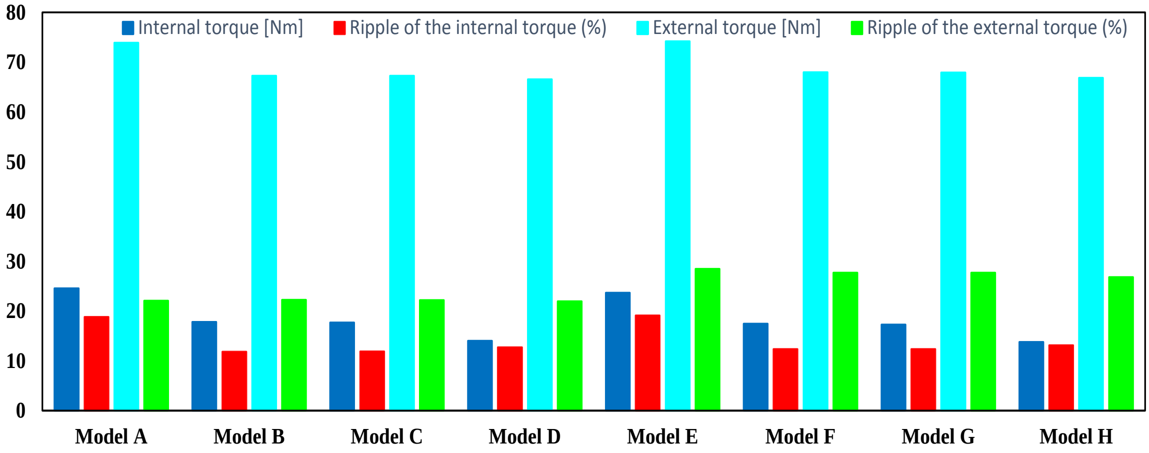

Fig. 7: Torque and torque ripple comparison for various suggested topologies.

The results in Table 4 show that Model B (hyperbolic reluctance rotor with surface PM) and Model C (hyperbolic-line reluctance rotor with surface PM) perform better than the other models. Model C was chosen as the optimal structure due to the following criteria:

- Low torque ripple: Model C, with an internal torque ripple of 11.88% and an external torque ripple of 22.24%, similar to Model B (11.87% and 22.26%), provides smoother performance, which is crucial for noise-sensitive underwater applications [15]. These values are significantly lower than those of models E, F, G, and H (internal ripple 12.36%-19.11% and external ripple 26.85%-28.49%), which is due to the greater air gap in the internal PM rotor [13].
- Balanced torque: Model C provides an internal torque of 17.7 Nm and an external torque of -67.27 Nm, which is similar to Model B but higher than Model D (14.03 and -66.59 Nm) and more balanced than Model A (24.61 and -73.92 Nm), which has a higher ripple (18.84%).
- Acceptable THD: The back EMF THD of model C (23.29%) is slightly higher than that of model B (20.20%), but considering the sinusoidal back EMF of the distributed winding, it is within an acceptable range and ensures stable performance [34]. The hyperbolic-line structure in Model C, with optimal magnetic flux distribution, reduces the primary harmonics of back EMF, which helps improve cogging torque [34].
- Appropriate efficiency: The efficiency of model C (87.36%) is similar to model B (87.30%) and higher than model A (86.15%), which is suitable for underwater applications with an output power of 8.90 kW [5], [15].
- Cogging torque optimization: Model C, with a cogging torque of 4.41 Nm, along with low torque ripple, facilitates the optimization of the cogging torque of the PM outer rotor in the later stages of design [34].

The surface PM rotor in models A to D offers better performance in CRDRSM compared to the internal PM rotor (models E to H) due to the smaller air gap and higher flux density [5]. Model C, with the combination of a hyperbolic-line reluctance rotor and a surface PM, was selected as the best structure for the proposed CRDRSM due to its balance between high torque, low ripple, reduced primary back EMF harmonics, and adequate efficiency. This structure is ideal for submarine propulsion applications that require smooth operation and low noise [5], [15].

Cogging Torque Optimization

As shown in Section 3, Model C (Hyperbolic-Line Reluctance Rotor with Surface PM Rotor) was selected as the optimal structure for CRDRSM due to the balance between high torque, low torque ripple, and adequate efficiency. However, the external torque ripple remains high, primarily due to cogging torque [16]. This section addresses the optimization of the cogging torque of model C using the Taguchi method for applications that require low noise levels [5], [15].

Fig. 8 shows the flowchart of the CRDRSM optimization process. The main objective is to find the optimal design using a combination of comparing winding and different structures, using the Taguchi method, and FEA.

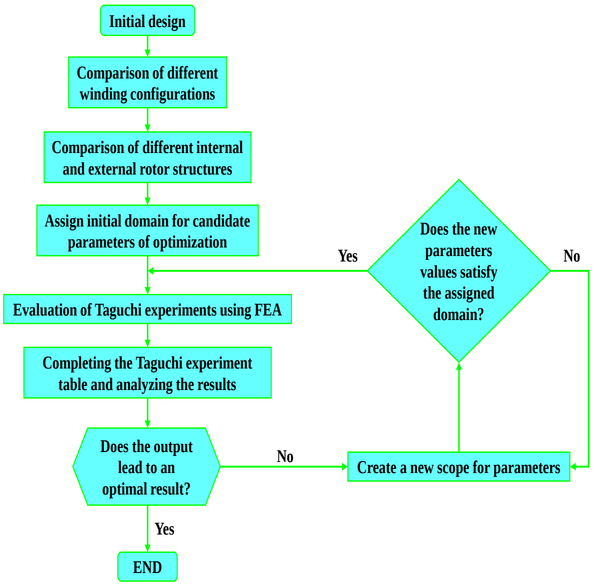

Fig. 8: Flowchart of CRDRSM optimization process.

The Taguchi method for optimizing the cogging torque of model C is applied using a five-level optimization structure. The process involves selecting initial parameters, evaluating results, and adjusting the parameter ranges until the desired outcome is achieved.

The starting point of the process is the initial design of the motor based on the performance specifications. After selecting suitable types of winding and rotor structures for the proposed CRDRSM based on the analyses in section 3, then the effective geometric parameters and their range of variations are determined so that the effect of each parameter on cogging torque can be analyzed through FEA simulation. Finally, the data obtained from the simulation are entered into the Taguchi matrix and processed using statistical methods (such as analysis of variance). If the results do not improve, the previous range must be adjusted, a new range defined, and the Taguchi optimization repeated to achieve optimal results.

A. Determining Optimization Goals and Optimization Factors

Considering the needs of high-torque, low-noise, and efficient drives [5], [15], cogging torque was chosen as the main optimization target, as its reduction directly improves torque ripple and acoustic noise [16]. Four design variables, including the PM arc angle, PM thickness, stator slot opening, and stator tooth width, which significantly affect cogging torque, were selected. These four parameters are shown in Fig. 9.

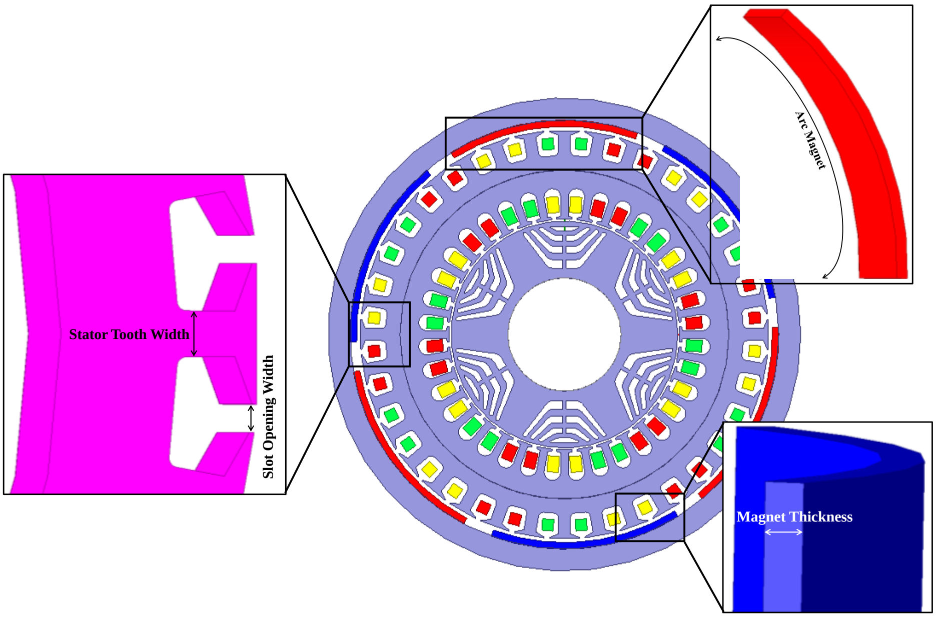

Fig. 9: Optimization parameters in the Taguchi method.

Table 5: Selection range of optimization parameters

Optimization Factor	Symbol	Design range	Range	Unit
Arc Magnet	Arc PM	$0.6 \leq \frac{\alpha_m}{\alpha_p} \leq 0.8$	[47 - 51]	deg
Magnet Thickness	MT	$\frac{B_g \cdot g}{B_r} \leq \mathrm{MT} \leq \frac{B_{sat} \cdot g}{B_r}$	[2.9 - 3.7]	mm
Slot Opening Width	SOW	$k_s \cdot \frac{2\pi R_{si}}{N_s}$	[3 - 5]	mm
Stator Tooth Width	STW	$\frac{\Phi}{B_{max} \cdot l_s}$	[4.8 - 6.4]	mm

B. Determining the Optimal Value Range and Level Value of the Optimization Factor

The range of optimization variables was determined using preliminary analyses in ANSYS Maxwell software, as shown in Table 5. Four levels of influence, which are within the range of the optimal value of each factor, are selected. Then, the five levels of values are sorted in ascending order according to the sorting principle and are sequentially named as levels 1, 2, 3, 4, and 5. The values of each level are shown in Table 6.

Table 6: Number of levels for the optimization factor

Symbol	Level 1	Level 2	Level 3	Level 4	Level 5
Arc PM	47	48	49	50	51
MT	2.9	3.1	3.3	3.5	3.7
SOW	3	3.5	4	4.5	5
STW	4.8	5.2	5.6	6	6.4

In Table 5, $\frac{\alpha_m}{\alpha_p}$ is the magnetic arc to pole angle ratio, B_g is the air gap flux density, B_{sat} is the magnet's saturation density, B_r is the magnet's residual flux, and g is the external air gap. N_s is the number of stator slots, $0.2 \leq k_s \leq 0.5$, and R_{si} is the stator yoke's inner radius. l_s is the effective length of the outer stator, B_{max} is the maximum allowable flux density in the tooth, and Φ is the flux flowing through the tooth.

In order to investigate the reduction of cogging torque due to various design variables, each design variable is parameterized in the optimization process, and the four parameters in Table 5 are selected as optimization variables.

The upper and lower bounds are provided according to Table 5; other parameters are fixed. After obtaining the cogging torque values in different models, the minimum values are selected to plot the trend of cogging torque changes with the parameters, and the optimal parameters are simulated in Maxwell for verification. If the optimal effect meets expectations, the optimization is complete. If the effect is not as expected, it is necessary to adjust the upper and lower limits of the parameters to optimize them.

In Table 7, in the columns of the experimental matrix, L_1 to L_5 refer to the Level 1 to Level 5 optimization coefficients specified in Table 6.

Considering four optimization factors (according to Table 5) and determining five levels for each optimization factor (according to Table 6), the orthogonal experiment table is designed as shown in Table 7.

Thus, to achieve motor optimization, only 25 tests (5^2=25) are needed, as the Taguchi method with the orthogonal table reduces the number of tests from 5^4=625 tests to 25 tests, significantly decreasing computation time [28], [29], [31].

Table 7: Orthogonal table and finite element simulation results

	Experimental matrix				Optimization Factor				Goals			
Exp. Num	Arc PM	SOW	MT	STW	Arc PM (deg)	SOW (mm)	MT (mm)	STW (mm)	Cogging zero-peak (Nm)	EMF(V)	THD (%)	P_{out} (KW)
1	L_1	L_1	L_1	L_1	47	3	2.9	4.8	11.12	225.64	21.97	8.21
2	L_1	L_2	L_2	L_2	47	3.5	3.1	5.2	10.94	220.19	21.92	8.49
3	L_1	L_3	L_3	L_3	47	4	3.3	5.6	11.08	216.08	21.91	8.76
4	L_1	L_4	L_4	L_4	47	4.5	3.5	6	11.94	212.78	21.91	8.75
5	L_1	L_5	L_5	L_5	47	5	3.7	6.4	13.3	210.63	21.93	8.82
6	L_2	L_1	L_2	L_3	48	3	3.1	5.6	4.3	209.48	21.75	8.91
7	L_2	L_2	L_3	L_4	48	3.5	3.3	6	7.85	209.88	20.15	8.78
8	L_2	L_3	L_4	L_5	48	4	3.5	6.4	9.04	207.54	20.15	8.86
9	L_2	L_4	L_5	L_1	48	4.5	3.7	4.8	12.78	215.63	21.83	8.95
10	L_2	L_5	L_1	L_2	48	5	2.9	5.2	13.22	223.16	21.82	8.69
11	L_3	L_1	L_3	L_5	49	3	3.3	6.4	5.25	204.33	20.24	8.85
12	L_3	L_2	L_4	L_1	49	3.5	3.5	4.8	6.27	212.69	20.31	8.93
13	L_3	L_3	L_5	L_2	49	4	3.7	5.2	8.63	207.06	20.28	9
14	L_3	L_4	L_1	L_3	49	4.5	2.9	5.6	11.15	214.91	20.27	8.57
15	L_3	L_5	L_2	L_4	49	5	3.1	6	12.64	212.6	20.26	8.78
16	L_4	L_1	L_4	L_2	50	3	3.5	5.2	3.31	203.53	18.79	8.92
17	L_4	L_2	L_5	L_3	50	3.5	3.7	5.6	5.15	199.93	18.77	8.94
18	L_4	L_3	L_1	L_4	50	4	2.9	6	6.18	207.97	18.78	8.68
19	L_4	L_4	L_2	L_5	50	4.5	3.1	6.4	7.52	206.31	18.77	8.82
20	L_4	L_5	L_3	L_1	50	5	3.3	4.8	7.34	215.07	18.85	8.93
21	L_5	L_1	L_5	L_4	51	3	3.7	6	1.69	194.14	18.87	8.81
22	L_5	L_2	L_1	L_5	51	3.5	2.9	6.4	1.71	201.98	18.87	8.7
23	L_5	L_3	L_2	L_1	51	4	3.1	4.8	3.6	210.6	18.92	8.84
24	L_5	L_4	L_3	L_2	51	4.5	3.3	5.2	2.34	205.67	18.91	8.97
25	L_5	L_5	L_4	L_3	51	5	3.5	5.6	2.23	202.52	18.9	8.96

C. Optimization Process and Result Analysis

Using the orthogonal table, 25 motor models were simulated in ANSYS Maxwell, and the cogging torque (zero to peak) for each combination was calculated (Table 7). The results were evaluated using the signal-to-noise ratio (SNR) and mean analysis [31]:

$$A = \frac{1}{n}\sum_{i=1}^{n} S_i \tag{12}$$

In (12), A is the average result of each optimization objective; n is the number of trials, n=25 in this article; and S_i is the i-th optimization objective value. (i is one of 1-25) [29].

Based on the analysis of the data in Table 7, and with the objective function being the reduction of cogging torque, the signal/noise ratio index is calculated using the Taguchi method so that lower values are preferred. The level with the highest average signal/noise ratio is selected as the optimal level for the objective function, as this level leads to the lowest value under noisy conditions with the highest stability. In addition to reducing the complexity of experiments, the Taguchi method increases the accuracy and stability of the optimization process and reduces the system's sensitivity to unwanted changes.

The Taguchi method establishes an optimal balance between all criteria by analyzing the signal/noise ratio and the average effect of each parameter and provides the optimal model through a systematic approach [26], [27].

The final best combination of motor main parameters and the comparison results of performance indexes before and after optimization are shown in Table 9 and Table 10.

The results in Table 10 show that the cogging torque has improved from 4.41 Nm to 1.66 Nm (a reduction of 62.36%), which is consistent with the impact of the optimized variables (Arc PM, SOW, MT, STW) [16]-[18].

Table 8: Average results for each optimization objective

-	Cogging $_{\text{zero-peak}}$	EMF	THD	P_{out}
A	7.62 Nm	210.01 V	20.2 %	8.8 KW

Table 9: Optimization factor parameters before and after optimization

Parameter	Arc PM	SOW	MT	STW
Before optimization	52 deg	3 mm	3.4 mm	6.4 mm
After optimization	51 deg	3 mm	3.3 mm	5.6 mm

Table 10: Comparison of various performance indexes before and after optimization

Parameter	Before optimization	After optimization	Unit
Cogging $_{\text{zero-peak}}$	4.41	1.66	Nm
Ripple Torque $_{\text{Internal}}$	11.88	10.16	%
$P_{\text{out-put}}$	8.9	8.94	KW
THD Voltage $_{\text{NL}}$	23.29	18.39	%
EMF $_{\text{rms}}$	193.04	199.69	V
η	87.36	88.27	%

The THD of the back EMF decreased from 23.29% to 18.39%, indicating an improvement in the back EMF harmonics due to the optimal flux distribution in the hyperbolic-line structure [18]. The internal torque ripple (10.16%), output power (8.94 kW), and efficiency (88.27%) also improved, which aligns with the requirements of submarine drives (low noise, high torque) [5], [15]. These results confirm the effectiveness of the Taguchi method in reducing cogging torque while maintaining the overall performance of the motor [28], [29], [31].

Simulation Results Analysis

In this section, the performance characteristics of the optimized model C for CRDRSM have been evaluated using two-dimensional FEA in ANSYS Maxwell software. The simulation results for the inner and outer rotors have been presented to confirm the performance of the optimized model C as the best choice [5], [15].

A. Magnetic Flux Density Distributions

The distribution of magnetic flux density of the proposed motor under nominal current at six different rotor positions is shown in Fig. 10.

The maximum flux density occurs at the inner poles of the stator and reaches 2.05 Tesla. No part of the stator or rotor iron layers reaches full saturation under nominal current, indicating the appropriate design of the magnetic structure to maintain stable performance [5], [18].

B. Air Gap Flux Density Analysis

Fig. 11 shows the comparative curves of air gap flux density for internal and external air gaps against rotor position.

It can be observed that the air gap flux density of the proposed PMSM is higher than that of the SRM. This increase in flux density is due to the use of PM in the outer rotor, which optimizes the flux distribution. This indicates the higher average torque potential of PMSM compared to SRM.

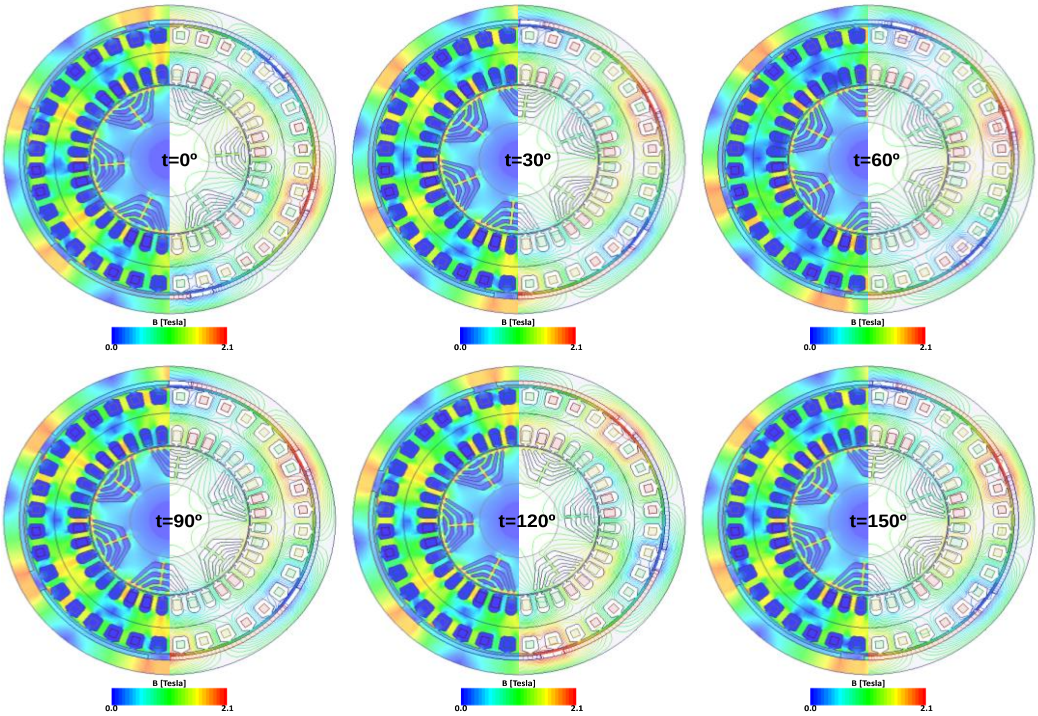

Fig. 10: Magnetic flux density and flux lines distributions of CRDRSM under current.

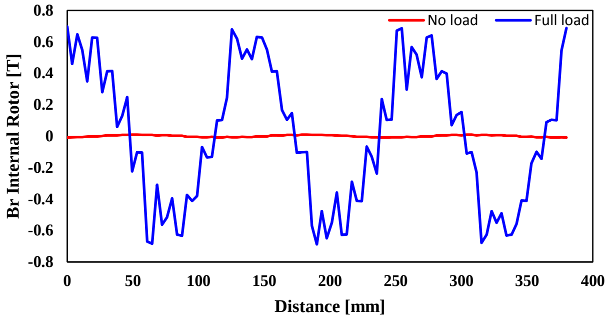

(a) Internal air gap

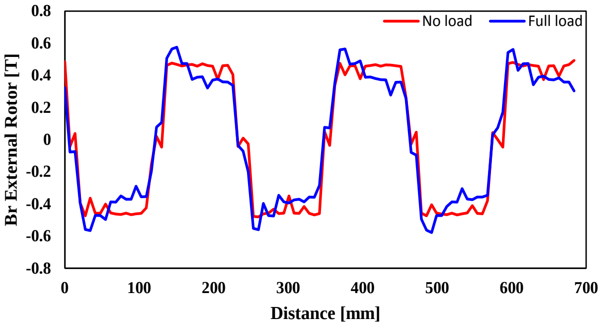

(b) External air gap

Fig. 11: Comparison of the air-gap flux densities for CRDRSM.

C. Output Torque Analysis

Fig. 12(a) shows the cogging torque curves versus time for the initial and optimized models, and Fig. 12(b) shows the output torque due to the inner rotor versus time. It is seen that by optimal selection of parameters Arc PM, SOW, MT, and STW, the cogging torque has been much decreased, with negligible effect on the value of internal rotor torque.

It can be observed that the torque difference between the two structures occurs near the rotor alignment position. This is because the air gap reluctances near the aligned positions of the rotors are smaller than the reluctances near the non-aligned positions of the rotors. Therefore, the PM flux near the aligned positions closes its path through the air gaps, increasing the air gap flux density and the output torque.

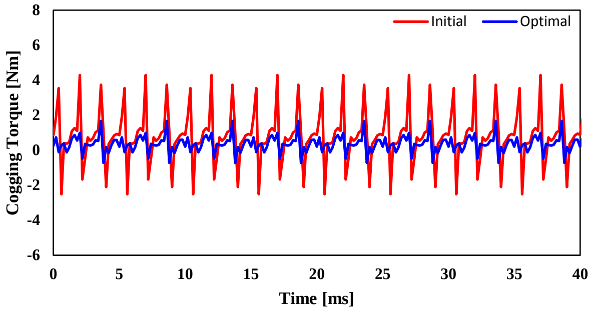

(a) Cogging torque

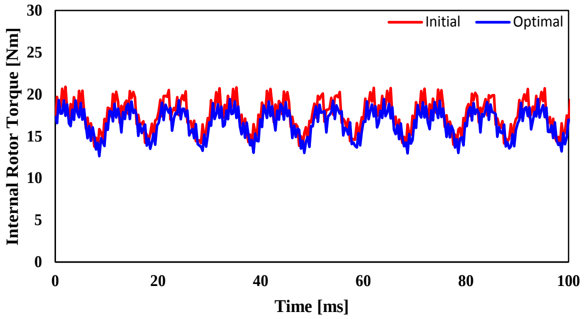

(b) Internal rotor torque

Fig. 12: Comparison of initial and optimal models for CRDRSM.

D. Comparison between the Initial Model and the Optimal Model

To evaluate the performance of the optimized model C, a comparison was made between the initial and optimal models based on key indicators. To ensure a fair comparison, the rated power, outer diameter, air gap length, and steel material were kept the same in both models. The comparison indices include cogging torque, average torque, torque ripple, RMS and THD of back EMF, RMS of phase current, output power, losses, and efficiency. The results are presented in Table 11.

Table 11: Comparison of the initial and the optimal models

Model	Initial	Optimal	Unit
Arc PM	52	51	Deg
SOW	3	3	mm
MT	3.4	3.3	mm
STW	6.4	5.6	mm
Cogging $_{zero\text{-}peak}$	4.41	1.66	Nm
Torque $_{Internal}$	17.7	16.55	Nm
Ripple Torque $_{Internal}$	11.88	10.16	%
Torque $_{External}$	-67.27	-68.91	Nm
Ripple Torque $_{External}$	22.24	26.04	%
First Harmonic $_{NL}$	116.8	102.81	V
THD Voltage $_{NL}$	23.29	18.39	%
EMF_{rms}	193.04	199.69	V
I_{rms}	18.97	19.42	A
$P_{out\text{-}put}$	8.9	8.94	KW
η	87.36	88.27	%

Analysis of results:

- Cogging torque: The reduction from 4.41 to 1.66 Nm (62.36%) indicates a significant improvement due to the optimization of design variables [16]-[18].
- Internal and external torque: The internal torque has slightly decreased (from 17.7 to 16.55 Nm), but the external torque has improved (from -67.27 to -68.91 Nm), which is consistent with the increase in air gap flux density [5].
- Torque ripple: The internal torque ripple has decreased from 11.88% to 10.16%, but the external torque ripple has increased from 22.24% to 26.04%. This increase may be due to changes in SOW and STW, which require further investigation [16].
- THD and EMF: The reduction in THD of back EMF (from 23.29% to 18.39%) and the increase in RMS of back EMF (from 193.04 to 199.69 volts) indicate an improvement in Back-EMF harmonics due to the Hyperbolic-Line structure [18].
- Efficiency and output power: The increase in efficiency (from 87.36% to 88.27%) and output power (from 8.90 to 8.94 kilowatts) is consistent with the requirements of submarines (low noise, high torque) [5], [15].
- Losses and current: A slight increase in RMS of current (from 18.97 to 19.42 amperes) is acceptable due to the improvement in torque and output power [5].

The optimized motor's output waveforms (cogging torque, stator current, output torque, and back-EMF) are displayed in Fig. 13. As shown in Fig. 13(a), the internal and external rotors generate steady average torques with opposite directions, confirming the intended counter-rotating operation. Compared with the initial design, the internal torque slightly decreases, whereas the external torque increases, which is consistent with the enhanced air-gap flux density and improved electromagnetic coupling in the optimized structure. Although the external rotor exhibits higher torque ripple due to its larger effective radius and slot–magnet interaction, the overall torque production remains stable and suitable for high-torque applications. Fig. 13(b) presents the cogging torque waveform of the optimized model. A significant reduction in cogging torque is achieved. This improvement is mainly attributed to the optimization of stator and rotor geometrical parameters, which effectively mitigates slotting effects and magnetic reluctance variation. The reduced cogging torque is particularly advantageous for low-noise and low-vibration operating conditions, such as underwater propulsion systems. The three-phase back-EMF waveforms shown in Fig. 13(c) exhibit good symmetry and a sinusoidal shape with a 120° phase displacement, indicating balanced electromagnetic behavior. Results demonstrate an improvement in back-EMF harmonic quality, which can be attributed to the optimized rotor geometry and the hyperbolic-line structure that smooths the air-gap flux distribution. Fig. 13(d) shows the stator current waveforms under rated operating conditions. The phase currents are balanced and sinusoidal, indicating stable machine operation and proper electromagnetic design. No noticeable current distortion is observed, confirming that the optimized design does not introduce adverse electromagnetic effects. As a result, the suggested PMSM generates more torque than the suggested SRM. Actually, the suggested motor builds an effective structure that provides optimal performance and high torque. The optimum option for the suggested CRDRSM in underwater applications is the optimized model C because of its low cogging torque, high efficiency, and appropriate torque [5], [12], [15], [36].

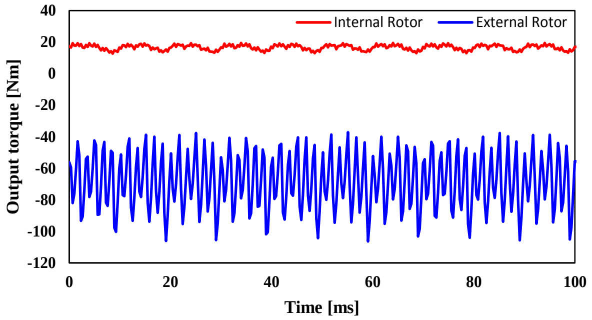

(a) Output torque

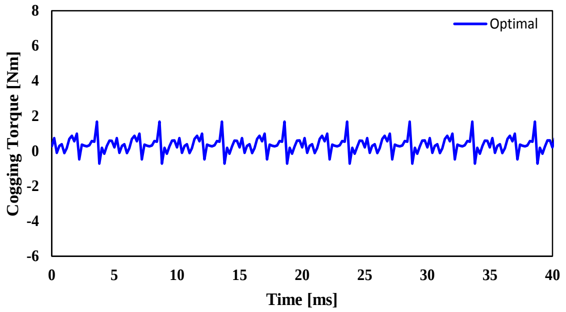

(b) Cogging torque

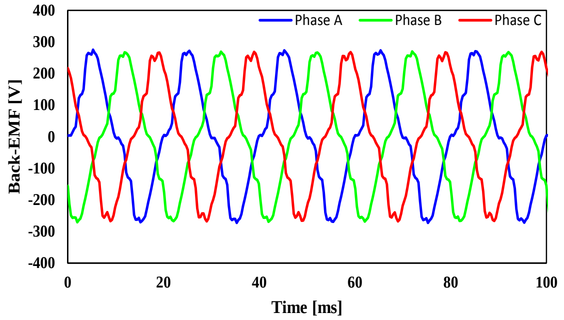

(c) Back-EMF

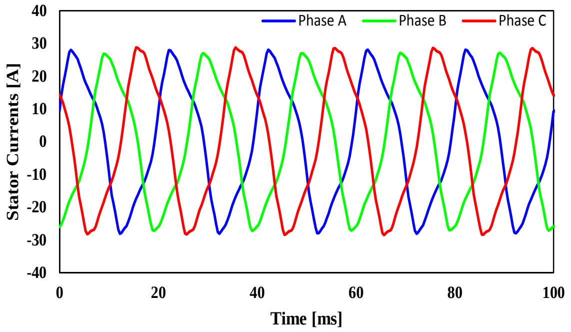

(d) Stator current

Fig. 13: Specifications of the optimal model for CRDRSM.

Conclusion

In this study, a CRDRSM is proposed that uses a common stator configuration, an external PM rotor, and an internal reluctance rotor. Based on FEA simulations, it was shown that the distributed winding provides the best result among all the examined windings. Then, using the distributed winding and with the aim of selecting the optimal structure among the proposed topologies, the combination of the inner rotor (reluctance) and the outer rotor (PM) for the proposed CRDRSM was designed and evaluated. The results showed that Model C, with the combination of the hyperbolic-line reluctance rotor and the surface PM, was chosen as the best structure for the CRDRSM. Model C is ideal for submarine propulsion applications that require smooth operation and low noise due to its balance between high torque, low ripple, reduced primary back-EMF harmonics, and adequate efficiency. To reduce cogging torque, which is the main factor causing torque ripple and acoustic noise, the optimization of the motor's geometric dimensions was carried out using the Taguchi method combined with FEA. After optimization, the cogging torque was reduced by 62.36% from 4.41 Nm to 1.66 Nm due to the optimization of design variables. Additionally, the ripple torque of the inner rotor and the THD of back EMF were reduced, and the output power and efficiency of the proposed motor were increased, which aligns with the requirements for submarines (low noise, high torque). Additionally, the electromagnetic performance of the proposed motor (CRDRSM) in terms of flux densities, output torques, and cogging torque was confirmed.

Author Contributions

P. Nadri carried out the design, modeling, simulation and writing. B. Rezaeealam performed the conceptualization, supervision and writing. M. Mikhak-Beyranvand investigated the results.

Acknowledgment

We gratefully acknowledge the editorial team of JECEI and the referees who helped the authors in publishing this article.

Conflict of Interest

The authors declare no potential conflict of interest regarding the publication of this work. In addition, the ethical issues, including plagiarism, informed consent, misconduct, data fabrication and/or falsification, double publication and, or submission, and redundancy, have been completely witnessed by the authors.

Funding

This research received no external funding.

Abbreviations

CRDRSM	Counter-Rotating Dual-Rotor Synchronous Motor
PM	Permanent Magnet
FEA	Finite Element Analysis
PMSM	Permanent Magnet Synchronous Motor
SRM	Switched Reluctance Motor
EMF	Electromotive Force
SynRM	Synchronous Reluctance Motor

THD	Total Harmonic Distortion
SOW	Slot Opening Width
MT	Magnet Thickness
STW	Stator Tooth Width

References

[1] W. Ullah, F. Khan, U. B. Akuru, B. Khan, S. A. Khalil, "Evaluation of counter-rotating dual-rotor permanent-magnet flux-switching machine with series and parallel stator teeth," Machines, 11(11): 989, 2023.

[2] B. Virlan, A. Munteanu, L. Livadaru, A. Bobu, I. Nacu, A. Simion, "Dual rotor radial flux concentrated wound permanent magnet synchronous machine with high power density," Adv. Electr. Comput. Eng., 23(4): 41-50, 2023.

[3] T. Zou, D. Li, R. Qu, J. Li, D. Jiang, "Analysis of a dual-rotor, toroidal-winding, axial-flux vernier permanent magnet machine," IEEE Trans. Ind. Appl., 53(3): 1920-1930, 2017.

[4] W. Ullah, F. Khan, U. B. Akuru, M. Yousuf, "Magnetic coupling effect and performance analysis of dual rotor permanent magnet flux switching generator for counter rotating wind power generation," IEEE Trans. Energy Convers., 38(4): 2895-2908, 2023.

[5] G. Liu, G. Qiu, J. Shi, F. Zhang, "Study on counter-rotating dual-rotor permanent magnet motor for underwater vehicle propulsion," IEEE Trans. Appl. Supercond., 28(3): 1-5, 2018.

[6] F. Kutt, K. Blecharz, D. Karkosiński, "Axial-flux permanent-magnet dual-rotor generator for a counter-rotating wind turbine," Energies, 13(11): 2833, 2020.

[7] M. Yang, Z. Zhong, Q. Wang, Z. Shao, "An analytical model for stator yokeless radial flux dual rotor permanent magnet synchronous machine," COMPEL-The Int. J. Comput. Math. Electr. Electron. Eng., 41(5): 1920-1939, 2022.

[8] H. Ouldhamrane, J. F. Charpentier, F. Khoucha, A. Zaoui, Y. Achour, M. Benbouzid, "Optimal design of axial flux permanent magnet motors for ship RIM-driven thruster," Machines, 10(10): 932, 2022.

[9] A. Ghayth, M. Şimşir, "Recent trends and challenges of electric motor technologies," Int. J. Electr. Eng. Sustain., 1(2): 21-28, 2023.

[10] L. Ananda Padmanaban, P. Saravanan, "Design, analysis and comparison of switched reluctance motors for electric vehicle application," Automatika: časopis za automatiku, mjerenje, elektroniku, računarstvo i komunikacije, 64(2): 239-247, 2023.

[11] W. S. Jung, H. K. Lee, Y. K. Lee, S. M. Kim, J. I. Lee, J. Y. Choi, "Analysis and comparison of permanent magnet synchronous motors according to rotor type under the same design specifications," Energies, 16(3): 1306, 2023.

[12] X. Kong, Y. Zhang, G. Xu, "Optimal design and control of permanent magnet assisted dual rotor motor," Front. Energy Res., 11: 1240473, 2023.

[13] C. Babetto, G. Bacco, N. Bianchi, "Synchronous reluctance machine optimization for high-speed applications," IEEE Trans. Energy Convers., 33(3): 1266-1273, 2018.

[14] T. Guo, N. Schofield, A. Emadi, "Double-rotor switched reluctance machine with segmented rotors," ed: Google Patents, 2019.

[15] B. Cheng, S. Pang, H. Ou, Z. Hu, Z. Mao, "Comparative research on topologies of contra-rotating motors for underwater vehicles," J. Mar. Sci. Eng., 11(11): 2042, 2023.

[16] W. Tong, S. Li, X. Pan, S. Wu, R. Tang, "Analytical model for cogging torque calculation in surface-mounted permanent magnet motors with rotor eccentricity and magnet defects," IEEE Trans. Energy Convers., 35(4): 2191-2200, 2020.

[17] A. Patel, "Slot opening displacement technique for cogging torque reduction of axial flux brushless DC motor for electric two-wheeler application," Electr. Eng. Electromech., (2): 7-13, 2023.

[18] Y. J. Won et al., "Transfer learning-based design method for cogging torque reduction in PMSM with step-skew considering 3-D leakage flux," IEEE Trans. Magn., 59(11): 1-5, 2023.

[19] J. Wu, X. Zhu, Z. Xiang, D. Fan, L. Quan, L. Xu, "Robust optimization of a rare-earth-reduced high-torque-density PM motor for electric vehicles based on parameter sensitivity region," IEEE Trans. Veh. Technol., 71(10): 10269-10279, 2022.

[20] M. Vatani, A. Ghaffarpour, M. A. Jalali Kondelaji, M. Mirsalim, "Study of a modular toothed linear hybrid reluctance motor with permanent magnets in translator slots," IEEE Trans. Transport. Electrif., 8(3): 3554-3567, 2022.

[21] Y. Shimizu, S. Morimoto, M. Sanada, Y. Inoue, "Automatic design system with generative adversarial network and convolutional neural network for optimization design of interior permanent magnet synchronous motor," IEEE Trans. Energy Convers., 38(1): 724-734, 2022.

[22] K. S. Kim, B. H. Lee, "Taguchi robust design for the multi-response considering the manufacturing tolerance used in high-speed air blower motor," IET Electr. Power Appl., 14(7): 1141-1147, 2020.

[23] D. Xiang, Z.Q. Zhu, D. Liang, L. Mao, X. Qiu, S. Li, L. Zheng, "Taguchi-Based pre-process strategy for fast evaluating worst-case cogging torque due to PM tolerance interactions," IEEE Trans. Transport. Electrif., 11(1): 4097-4110, 2024.

[24] X. Kong, Z. Yang, "Multi-objective optimization of dual-stator permanent magnet motor based on composite algorithm," Sci. Rep., 15(1): 22982, 2025.

[25] M. A. Khioon, K. A. Hubeatir, M. M. AL-Khafaji, "Parametric optimization of laser conduction welding between stainless steel 316 and polyethylene terephthalate using taguchi method," Eng. Technol. J., 40(12): 1642-1649, 2022.

[26] A. Freddi, M. Salmon, "Introduction to the taguchi method," in Design principles and methodologies: from conceptualization to first prototyping with examples and case studies: Springer, 159-180, 2018.

[27] R. Davis, P. John, "Application of taguchi-based design of experiments for Industrial Chemical Processes,"in Statistical Approaches With Emphasis on Design of Experiments Applied to Chemical Processes. InTech, 137, 2018.

[28] P. Nadri, M. R. Besmi, "Design and optimization of permanent magnet flux-switching generator arrangement spoke by taguchi method for direct-drive wind turbines," AUT J. Electr. Eng., 56(1): 113-124, 2024.

[29] C. Qu, Z. Guo, Y. Hu, X. Wang, F. Han, "Multi-objective optimization design of a new permanent magnet synchronous motor based on the Taguchi method," Energies, 15(19): 7347, 2022.

[30] Y. Yu et al., "Multi objective optimization of permanent magnet synchronous motor based on taguchi method and PSO algorithm," Energies, 16(1): 267, 2022.

[31] S. R. Karimpour, M. R. Besmi, S. M. Mirimani, "Optimal design and verification of interior permanent magnet synchronous generator based on FEA and Taguchi method," Int. Trans. Electr. Energy Syst., 30(11): 12597, 2020.

[32] J. F. Gieras, Permanent magnet motor technology: design and applications. CRC press, 2009.

[33] H. Qiu, Y. Zhang, C. Yang, R. Yi, "Performance analysis and comparison of PMSM with concentrated winding and distributed winding," Archives Electr. Eng., 69(2): 303-317, 2020.

[34] Z. Azar, Z. Zhu, "Performance analysis of synchronous reluctance machines having nonoverlapping concentrated winding and

sinusoidal bipolar with DC bias excitation," IEEE Trans. Ind. Appl., 50(5): 3346-3356, 2014.

[35] A. EL-Refaie, M. Shah, "Induction machine performance with fractional-slot concentrated windings," COMPEL- Int. J. Comput. Math. Electri.Electron. Eng., 31(1): 119-139, 2011.

[36] A. Ghaffarpour, M. Mirsalim, "Split-tooth double-rotor permanent magnet switched reluctance motor," IEEE Trans. Transport. Electrif., 8(2): 2400-2411, 2022.

Biographies

Pouria Nadri received the B.Sc. degree in electrical engineering from Lorestan University, Khorramabad, Iran, in 2020, and the M.Sc. degree in electrical engineering from Shahed University, Tehran, Iran, in 2022. He is currently a Ph.D. candidate in electrical engineering at Lorestan University, Khorramabad, Iran. His research interests include design, optimization and analysis of electrical machines, power electronics, modeling and design using FEM, and electromagnetic modeling.

- Email: nadri.po@fe.lu.ac.ir
- ORCID: 0000-0002-8547-4007
- Web of Science Researcher ID: N/A
- Scopus Author ID: 59557771400
- Homepage: N/A

Behrooz Rezaeealam received the B.S. degree from Isfahan University of Technology in 1997, the M.S. and Ph.D. degrees from University of Tehran in 2000 and 2005, respectively, all in electrical engineering. He is currently an associate professor in the department of electrical engineering, Lorestan University, Iran. His research interests include modeling and design using FEM, electrical machines and drives.

- Email: rezaee.bh@lu.ac.ir
- ORCID: 0000-0002-9391-4826
- Web of Science Researcher ID: N/A
- Scopus Author ID: 9742086900
- Homepage: N/A

Morteza Mikhak-Beyranvand received the B.Sc. degree in Electrical Engineering from Hadaf University, Iran, in 2010, the M.Sc. degree in Electrical Engineering from Malek-Ashtar University of Technology, Iran, in 2013, and the Ph.D. degree in Electrical Engineering from Lorestan University, Iran, in 2019. He is currently an Assistant Professor with the Department of Electrical Engineering, Technical and Vocational University (TVU), Iran. His research interests include the design and analysis of electrical machines, power electronics, and electromagnetic–thermal modeling of power transformers. Recently, he has also started research and studies in the field of batteries, particularly battery lifetime estimation.

- Email: mbeyranvand@tvu.ac.ir
- ORCID: 0000-0002-5411-9918
- Web of Science Researcher ID: N/A
- Scopus Author ID: 57209781633
- Homepage: N/A